Environmental Earth Sciences (2024) 83:146
https://doi.org/10.1007/s12665-024-11451-2

ORIGINAL ARTICLE

Multiphysics monitoring of cementation operation: implications for wellbore integrity and hydrogeological characterization

Nima Gholizadeh Doonechaly[1] · Andreas Reinicke[1] · Marian Hertrich[1] · Katrin Plenkers[1,3] · Anne Obermann[1,2] · Frank Fischli[4] · Hansruedi Maurer[1] · Stefan Wiemer[2] · Domenico Giardini[1]

Received: 18 November 2022 / Accepted: 26 January 2024 / Published online: 28 February 2024

Abstract

The application of optical fibers for assessing cemented wellbore's integrity attracted considerable attention recently, because of low cost, decent temporal/spatial resolution and absence of downhole electronics. This study presents an integrated approach to compare measurements from distributed temperature sensing (DTS), distributed strain sensing (DSS) and fiber Bragg grating (FBG), at different stages of the wellbore cementation at Bedretto Underground Laboratory for Geosciences and Geoenergies. Before the cementation, the measurements from DTS provided information about the hydrogeological settings of the wellbore, including the major flow zones, and presence of a highly conductive hydraulic shortcut to a nearby wellbore. During the cement injection, the temperature sensors (DTS and temperature FBG) clearly detected the evolution of the top of the cement. While the mechanical deformation sensors (DSS and strain FBG) did not provide significant insights during this stage, their role became more pronounced in subsequent phases. Results show that the irregularities on the wall have minor influence on the thermo-mechanical response of the wellbore, both during and after cementation. After cementation, the temperature sensors (DTS and temperature FBG) traced different phases of cement-hardening process, while DSS measurements identified areas of major deformation, primarily in fracture/fault zones. It was also observed that localized elevation of temperature and extensional deformation along the wellbore during the cement-hardening are correlated with the presence of permeable structures, most likely due to continuous supply of water. Results of this study show that monitoring of the cemented wellbores using optical fibers, in particular during cement hardening, not only can be used to efficiently assess the wellbore integrity but also can provide us additional important information about the hydrogeological settings of the target reservoir volume.

Keywords Wellbore integrity · Optical fiber · Thermo-hydro-mechanical wellbore monitoring · Flow zone · Fracture

Introduction

The efficient exploitation of subsurface reservoirs requires wellbores with mitigated fluid/gas migration, appropriate mechanical and hydraulic barriers, and a long lifetime. This set of criteria is also referred to as wellbore integrity (Kiran et al. 2017; Manceau et al. 2015), which is addressed to a great extent by primary cementation of the wellbores. Therefore, it is important to verify the integrity of the cement in place (Cao et al. 2013). The potential factors that may (locally) compromise the cement integrity include among others; improper displacement of the drilling (or formation) fluid by the cement, sharp pressure/temperature changes in the wellbore after cementation, and carrying out operations in an already cased and cemented wellbore (Wu et al. 2017). The wellbore integrity is commonly investigated using wireline logging techniques, such as Cement Bond Log (CBL) (Pardue and Morris 1963), Variable Density Log (VDL) (Morris et al. 2003), and Ultra-Sonic Imaging Log (Thomas et al. 2016), based on which, the integrity of the cement to the casing, as well as to the formation, is evaluated (Kiran et al. 2017). However, the logging techniques (a) may lead to incorrect interpretation of the wellbore integrity if the

✉ Nima Gholizadeh Doonechaly
nima.gholizadeh@erdw.ethz.ch

1 Department of Earth Sciences, ETH, Zurich, Switzerland

2 Swiss Seismological Service (SED), ETH, Zurich, Switzerland

3 GmuG, Bad Nauheim, Germany

4 Marmota Engineering, Zurich, Switzerland

cement is locally contaminated within the wellbore (Batcheller 2013), (b) need access to the wellbore and c) can only be carried out after the cementation (Wu et al. 2017). To overcome such limitations, since mid-1990s, the application of fiber optics in subsurface characterization and evaluation gained considerable attention (Kamal 2014; Hurtig 1993). Such systems—in the forms of single-point, multi-point, or quasi-distributed (continuous) sensing configurations analyzed in time- or frequency-domain—can be used within the wellbore to measure temperature, strain, and vibration during the cementation process (Kragas et al. 2001). The reader is referred to the recent reviews on this topic for more information (Lindsey and Martin 2020; Zhu et al. 2017; Schenato 2017; Dakin et al. 1985).

The applications of the optical fiber in wellbore integrity monitoring includes: tracing the top of the cement during cementation operation (Reinsch et al. 2013), monitoring temperature changes and mechanical deformations during cement-hardening process and active monitoring of vibrations to evaluate cement bond to the formation/casing (Raab et al. 2019). As an example, Xue and Hashimoto (2017) used the distributed strain (DSS) and temperature (DTS) to evaluate wellbore- and caprock-integrity during CO_2 storage for different lithological layers along the wellbore. Wu et al. (2017) used optical fibers covered with a hydrocarbon sensitive polymer to measure the hydrocarbon migration along the cemented wellbore. Raab et al. (2019) used DTS (for identifying thermal signatures during cementation) and DAS (to record average-axial-strain amplitudes acquired during different well operations) to evaluate the cement placement and its coupling to the medium. The authors showed that the results from both technologies can be correlated with the observations from CBL. In another approach, Pearce et al. (2009) successfully utilized FBG system as a Real-Time Compaction Imager (RTCI) in a producing gas well, for casing strain monitoring during key well activities, including cementing, perforating, fracturing, and the start of production, demonstrating its ability to detect and interpret detailed responses. In a 2023 laboratory-scale experiment, Chen et al. (2023) validated the use of FBG technology as a promising, real-time, high-accuracy, and nondestructive tool for monitoring the integrity of cement sheaths, supported by an analytical model. To the best of the authors' knowledge, the potential of FBG technology for conducting high-frequency temperature sampling during field-scale cementation operations remains an area that has not been extensively investigated.

In terms of thermo-mechanical signatures, the cement hardening is considered as an exothermic reaction which can cause both expansion and contraction at different phases of hardening. The cement-hardening process can be divided into four major consecutive periods (Bullard et al. 2011): (a) initial reaction: involving dissolution and hydration of calcium silicate component in water, starting within seconds to a few minutes after the dissolution of cement, which can continue for several minutes, (b) slow reaction period: without significant heat generation, (c) acceleration period: associated with significant increase in heat generation (several mW/mg, depending the on the cement composition) due to nucleation and growth of the crystalized hydration products, and (d) deceleration period: associated with gradual decrease in generated heat which takes from days to several months. In this investigation, we present a comprehensive approach utilizing DTS, DSS, and FBG sensors to monitor wellbore integrity throughout the cementation process and subsequent hardening phases. Our study focuses on a 304-m-long geophysical monitoring wellbore (MB1) under challenging conditions, including the presence of hydraulic shortcuts and inflow zones. The main objectives of our research are to assess the performance and capabilities of these three sensor technologies for real-time monitoring of cementation processes and to shed light on the thermo-hydro-mechanical behavior of the wellbore during and after cement injection. By comparing and analyzing the data collected from these sensors, we aim to provide insights into the complex processes occurring within the wellbore, which can be used for better characterization of wellbore integrity and subsurface reservoirs.

Site description

BULGG, located at tunnel meter (TM) 2000 in the 5.2-km-long Bedretto tunnel in Ticino, Switzerland, is a research infrastructure developed by ETH Zürich as part of the Swiss Energy Strategy 2050 (SFOE 2021; Prognos 2012) to increase the share of the renewable geothermal energy (Rast et al. 2022; Keller and Schneider 1982). The detailed geological map and cross-section of the Bedretto tunnel are shown in Fig. 1 (Rast et al. 2022; Wenning et al. 2022; Keller and Schneider 1982). The Bedretto tunnel mainly consists of three geological units: the Tremola series (TM 0 to TM 434), the Prato series (TM 434 to TM 1138), and the Rotondo granite (TM 1138 to TM 5218) (Rast et al. 2022).

To-date, nine long wellbores have been drilled into the reservoir volume of the BULGG and completed for different purposes, namely: for monitoring (MB1, MB3, MB4, MB5, MB7 and MB8), characterization (MB2), and stimulation (ST1 and ST2), with measured depth ranges between 101 and 404 m and various inclinations (see Fig. 1c). For simplicity, all reported "depth" values in this study correspond to the "measured depth". A comprehensive review of the laboratory and the project, including the rock and hydrogeological characterization is provided by Ma et al. (2022). Numerous sensors have been deployed within the wellbores, incorporating a variety of sensor types, the overall

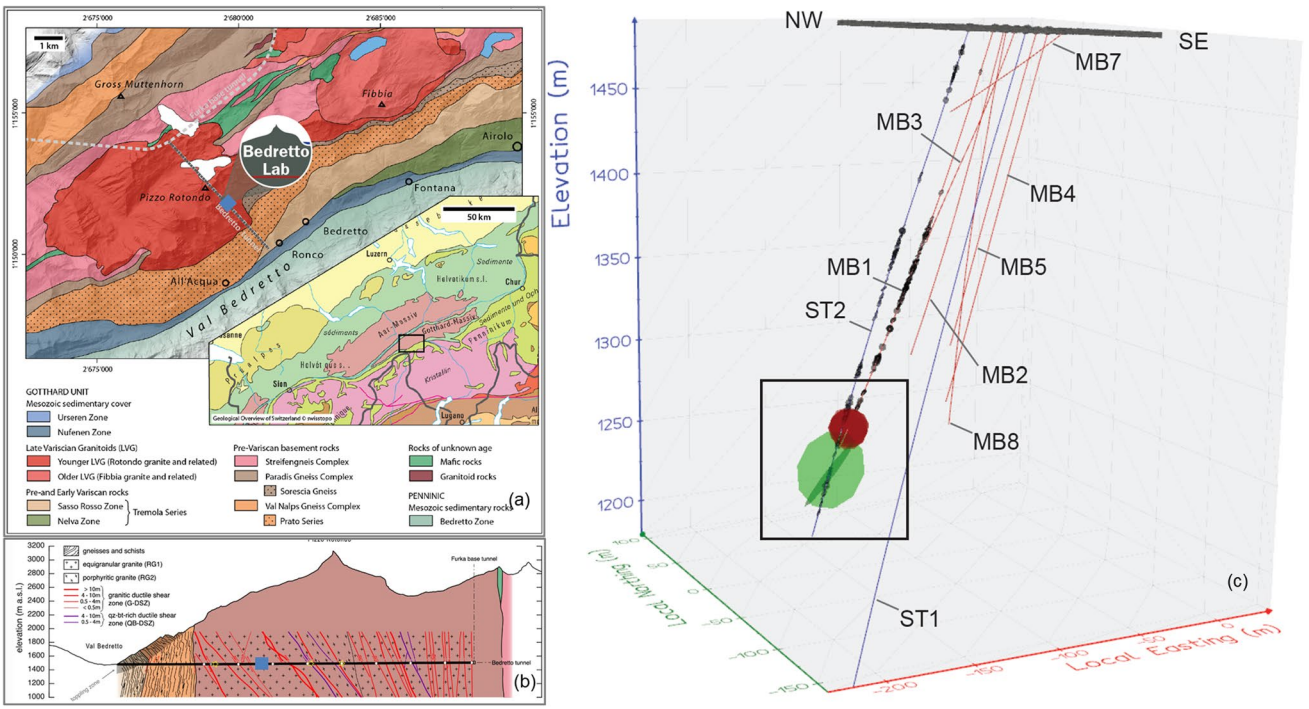

Fig. 1 **a** The geological map and **b** cross-section of the Bedretto tunnel with the BULGG marked with the blue rectangle as well as **c** the drilled wellbores in BULGG (the potential geometry of the detected hydraulic shortcut between the wellbore under study (MB1) and a nearby wellbore (ST2) is shown in the figure) [after (Rast et al. 2022; Wenning et al. 2022, Shakas et al. 2021, Keller and Schneider 1982)]

performance goals and installation procedure of which, are described in Plenkers et al. (2023). These include piezoelectric accelerometers, in-situ acoustic emission (AE) sensors, fiber-optic cables for distributed acoustic sensing (DAS), distributed strain sensing (DSS), distributed temperature sensing (DTS), Fiber Bragg Grating (FBG) sensors, geophones, ultrasonic transmitters, and pore pressure sensors. A comprehensive review of these sensors and their installation protocols are presented by Plenkers et al. (2023). As an additional advantage, some of the installed sensors, in particular, the DTS, DSS and FBG, provided us with the possibility to gain deeper insight into the hydrogeological settings of the target reservoir volume at the early stages of the project as well as to monitor the cementation operation in the wellbores with very high level of details (which is the focus of this study). The multi-sensor-network design was optimized to meet several installation challenges; namely relatively long and fractured wellbores, breakouts, relatively high pressure, and the requirement to cement the wellbore to assure wellbore integrity as well as to provide appropriate coupling between the sensors and the reservoir volume. A borehole specific cement design was developed in this context as described in detail by Plenkers et al. (2023). A central rod system was used in all wellbores for: (a) cement injection, and (b) mounting and fixation of all monitoring equipment for correct positioning. The FBG sensors were attached to the central rod using special brackets and spacers, while the fiber-optic cables (DTS and DSS) are fixated using a custom-made cable clamp approximately every 3 m (Plenkers et al. 2023). In addition, cable ties were used for further support in between. A schematic representation of the clamping systems used for distributed fiber cables and FBG sensors are presented in Fig. 2.

MB1 wellbore

The MB1 wellbore, which is the focus of this study, is drilled at tunnel meter 2050 m with a diameter of 16.5 cm, the measured depth of 304 m and the average dip of 40.3°. From about 144 m to the bottom of the wellbore, several fractures and fault zones discharge water with a total wellhead outflow of 9.5 l/min, measured immediately before cementation. MB1 is equipped with two separate DTS optical fiber lines (both multimode with the type 50/125 µm), one of which covers the full length of the wellbore, whereas the second fiber only extends to the depth of 263 m. The measurements from the longest installed DTS cable are only presented in this study. There exist two separate chains of FBG long-gauge sensors in MB1, each of which, consists of 10 sensors (20 in total). Each FBG sensor has a base length of 1 m. The single-mode DSS fiber, which comes with corrugated

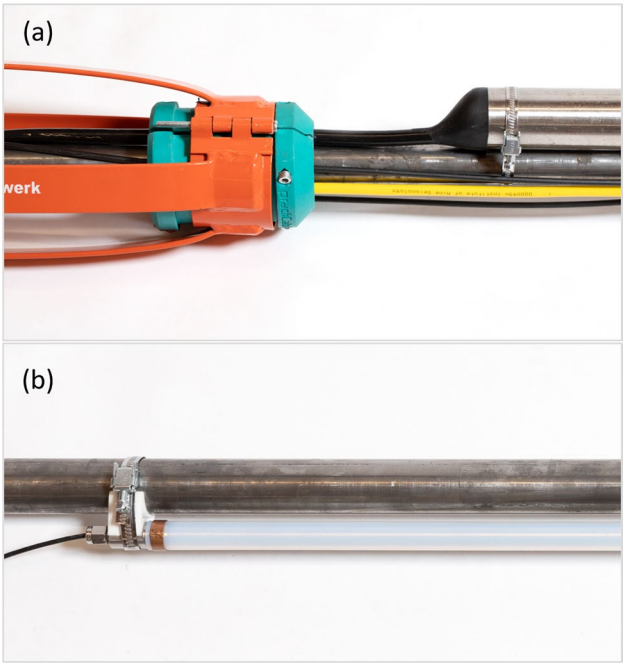

Fig. 2 **a** The centralizers with integrated clamps for (fiber) cables, and **b** special clamping system used for mounting FBG sensors on the central rod, [after Plenkers et al. (2023)]

surface for improved mechanical coupling to the wellbore wall, covers the full length of the wellbore.

The well logging results for temperature (and its gradient), fluid conductance (and its gradient), and the gamma ray (GR) measurements in MB1, smoothed using Savitzky–Golay filter with a smoothing window of 5 m, are shown in Fig. 3. Based on the temperature log, seven thermal anomalies, representing flowing zones, are manually identified in MB1, at the depths of 144 m, 182 m, 186 m, 214 m, 244 m, 278 m, and 290 m, out of which, all except the structure at 278 m, are characterized as heat loss zones. It is worth noting that these measured depths are reported with a 1 m resolution to conservatively cover the depth range over which the corresponding thermal anomaly is identified. The GR profile also shows a major anomaly at the depth of approximately 15 m, which is the bottom depth of the metallic conductor pipe installed in MB1. The temperature log data show an average geothermal gradient of about 10 °C/km along MB1, with a slight decreasing trend with increasing depth. This is partly caused by the thermal drainage of the reservoir volume by the tunnel boundary effect after being excavated. The wellbore breakout zones in MB1 are mainly identified between the depths of 150 m and 210 m (Ma et al. 2022).

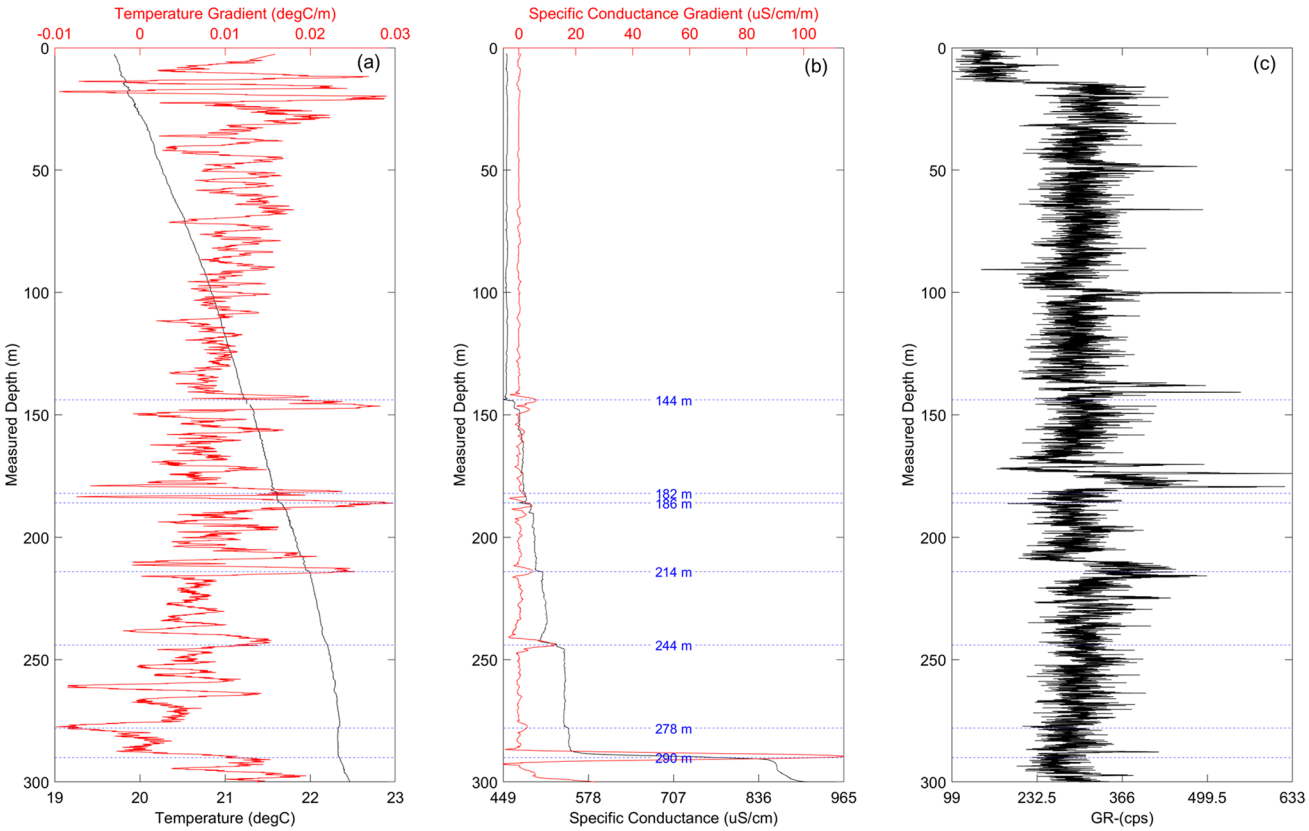

Fig. 3 The geophysical well logging results for: temperature and its gradient (**a**), fluid conductance and its gradient (**b**) and the GR (**c**) along the depth in MB1. The location of the potential flow zones are marked with dashed blue horizontal lines in all figures

After the logging and prior to the cementation operation, the wellhead of MB1 was closed, and consequently reached a stabilized pressure of 25.3 bar after 5 days. Next, a depressurization experiment was carried out, by partially opening the wellhead and monitoring the temporal evolution of the temperature profile along the wellbore using Silixa XT DTS instrument (Silixa XT 2023) with sampling frequency of 0.2 Hz. In this study, all the DTS raw data are processed using the code developed by Oregon State University's Center for Transformative Environmental Monitoring Programs' (CTEMP) Matlab DTS Toolbox (https://ctemps.org/data-processing) (CTEMPs 2015). The recorded wellbore pressure and temperature (as well as their time derivative and gradient) are presented in Fig. 4. Immediately after opening the wellbore, the temperature distribution (Fig. 4b) shows a distinct signature of colder fluid entering the wellbore at the depth of about 144 m, with an upward velocity of ca. 5.5 cm/s, indicating a total corresponding wellbore outflow of ca. 1.1 l/s, shortly after opening (estimated based on the wellbore diameter). The detected anomaly can also be clearly observed from the temperature's time-derivative plot (Fig. 4c). The temperature's time-derivative also shows a minor anomaly approximately at the depth of 240 m. The temperature gradient (Fig. 4d), however, provides a more pronounced representation of the thermal anomalies at 144 m, 244 m and 278 m, which are in good agreement with the well logging results (above mentioned). The thermal anomaly at 144 m is detected even before the well opening. The observed effects provided us with essential insights into fluid flow dynamics and temperature variations within the wellbore, which is of importance during the well cementation phases, including selection of cement slurry, additives, and pumping parameters.

A hydraulic shortcut between MB1 and ST2 (Fig. 1c) had been identified based on an injection test—over two cycles with a brief stop in between—that was carried out in ST2 using a straddle packer at the depth interval of 313.6–319.6 m, which resulted in a thermal anomaly in MB1 in the depth range of approximately between 276 and 290 m after 6 h of injection (Wenning et al. 2022), detected using the installed DTS in MB1. The inferred geometry of the hydraulic shortcut between the two wells is presented in Fig. 1b and the details of the experiment in provided by Wenning et al. (2022).

A pumping test was carried out in MB1, based on which, the transmissivity of MB1 was estimated as 2E–6 m^2/s (Ma et al. 2022). Before the cementation operation, MB1 was open to depressurize the reservoir volume, and an estimate

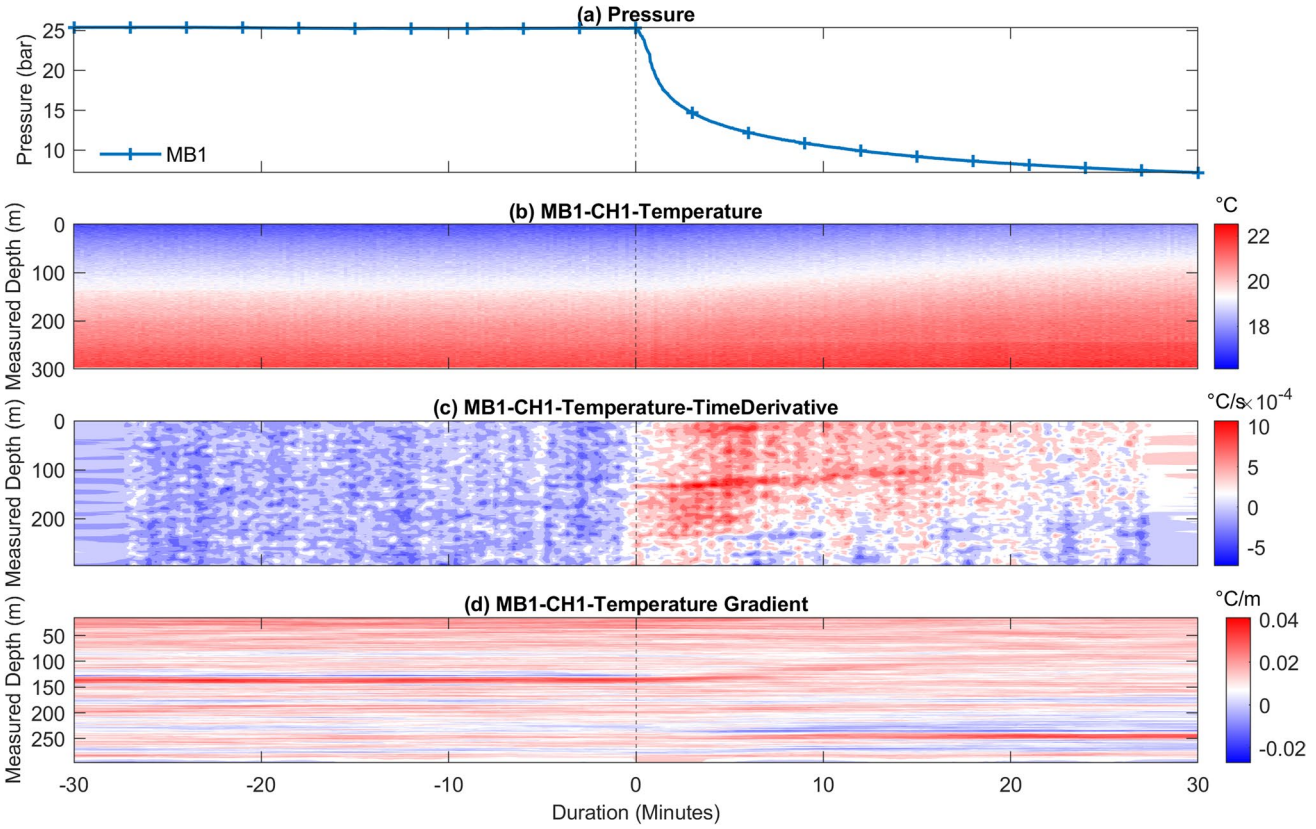

Fig. 4 **a**) Wellhead pressure, **b**) distributed wellbore temperature, **c**) temperature's time derivative and **d**) temperature gradient, during depressurization experiment in MB1

of the pressure built-up subsequent to a shut-in has been investigated by temporary wellhead closure. Wellhead pressure increases of approximately 7 bar and 13.5 bar have been recorded after 4 h and 24 h of closure, respectively, and noted for the cement slurry design conditions.

Methodology

During the MB1 cementation, the DTS was interrogated using Silixa Ultima DTS (Silixa ULTIMA 2023), with a spatial resolution of 0.125 m, temporal resolution of 20 s, and temperature resolution of 0.01 ˚C. The strain and temperature changes in FBG sensors were interrogated using a Micron Optics si255 Hyperion interrogator with a sampling rate of 10 Hz, a strain accuracy of 0.85 micro-strains (με) and a temperature accuracy of 0.05 °C. The DSS along the wellbore was read out by the Omnisens-Vision Dual distributed strain and temperature sensing system, with a spatial resolution of 0.5 m and a strain accuracy of < 2 με. Please note that the accuracies mentioned above are the read-out accuracies for a pure fiber. The sensors of all sensing types are protected and embedded in grout to connect to the host rock, which reduces the actual sensitivity of the system as a whole. Depending on the type of sensor protection and embedment, the actual accuracy/sensitivity usually is estimated at 10–20 με.

In this study, the compression is presented by negative values for the strain data. The strain measurements are corrected to exclude thermal effects, using the acquired temperature measurements at the corresponding sampling locations. The total strain for the FBG sensors in micro-strains (με) can be calculated according to Eq. (1) (Micron Optics 2014):

$$\Delta\varepsilon_{\text{tot}} = \frac{10^6}{F_G}\left\{\frac{\lambda_S - \lambda_{S,init}}{\lambda_{S,init}} - \frac{\lambda_T - \lambda_{T,init}}{\lambda_{T,init}}\right\} + \frac{\text{CTE}_T}{S_T}\cdot\frac{\lambda_T - \lambda_{T,init}}{\lambda_{T,init}} \quad (1)$$

where λ_S is the current wavelength in the strain FBG, $\lambda_{S,init}$ is the initial wavelength in the strain FBG, λ_T is the current wavelength in the temperature FBG, $\lambda_{T,init}$ is the initial wavelength in the temperature FBG, F_G and S_T are Gauge factor (c.f. calibration sheet), and CTE_T is the CTE of the FBG substrate.

Analogously, the formula for calculation of total strain in DSS sensors is represented by Eq. (2) (Horiguchi et al. 1995):

$$\Delta\varepsilon_{\text{tot}} = C_\varepsilon\left(\Delta\nu_S - \Delta T/C_T\right), \quad (2)$$

where C_ε is the strain coefficient (με/MHz), C_T is the temperature coefficient (°C/MHz), $\Delta\nu_s$ is the Brillouin frequency shift in the strain cable (MHz), and Δ_T is the change in temperature (°C). In this study, all the strain values as well as the temperature changes are set to zero at the beginning of the plotted monitoring period.

A CEM III furnace slag cement with a slurry density of 1.8 g/cm^3 was used for MB1 cementation which has low hydration heat and high strength. The pH of the CEM III drops to 12 shortly after initial hydration phase, so that a decomposition of rubber seals and cable materials is minimized. The Bentonite clay and SIKA UW Compound (SIKA 2023) (used as additives) have been optimized in a series of tests to reduce the formation of free water during hardening to minimum. A liquid cement fluidizer (Sikament 12A) was added to improve shear thinning behavior of the slurry for better pumpability. Also, several additional measures were taken to minimize the cement loss/dilution during and after cementation. The details of cement composition, properties and injection protocols are described in Plenkers et al. (2023)). Furthermore, Online Appendix A presents supplementary quantitative analysis aimed at mitigating cement loss.

During the cementation operation, the cement flow rate was monitored using two electromagnetic flowmeters at the inlet and outlet of MB1. Also cement properties, such as Marsh time, density and homogeneity at the return line (from the annulus) was monitored after injecting every 500 l of slurry. After the completion of the cementation operation, the MB1 wellhead was fully closed, and the wellhead pressure was continuously monitored.

Results

Monitoring during cementation

The results of monitoring MB1 during the cementation operation are shown in Fig. 5. In Fig. 5a, we can see that during the initial 15 min of injection, there is only a small increase in pressure, about 2 bar, at the wellhead, as indicated by the green arrow. However, as we continue to inject cement into the well, the pressure quickly rises to around 25 bar due to the rising cement column in the annulus. When we inject the second and third batches of cement slurry, we observe a pressure starts to decrease after about 1.5 h, as indicated by the blue arrow (it drops to 12 bar and then slightly increases) and a pressure starts to increase after about 3.25 h, as pointed by the red arrow (reaching 25–30 bar), respectively. Figure 5a also shows manually recorded data for the cement inflow and outflow, along with an estimate of cement loss in MB1, considering prior measurements of natural outflow. The natural inflow gradually decreases as the cement column in the annulus rises, eventually stopping after about 100 min of pumping (when the estimated height of the cement column in the annulus of MB1 is about 130 m). After this point,

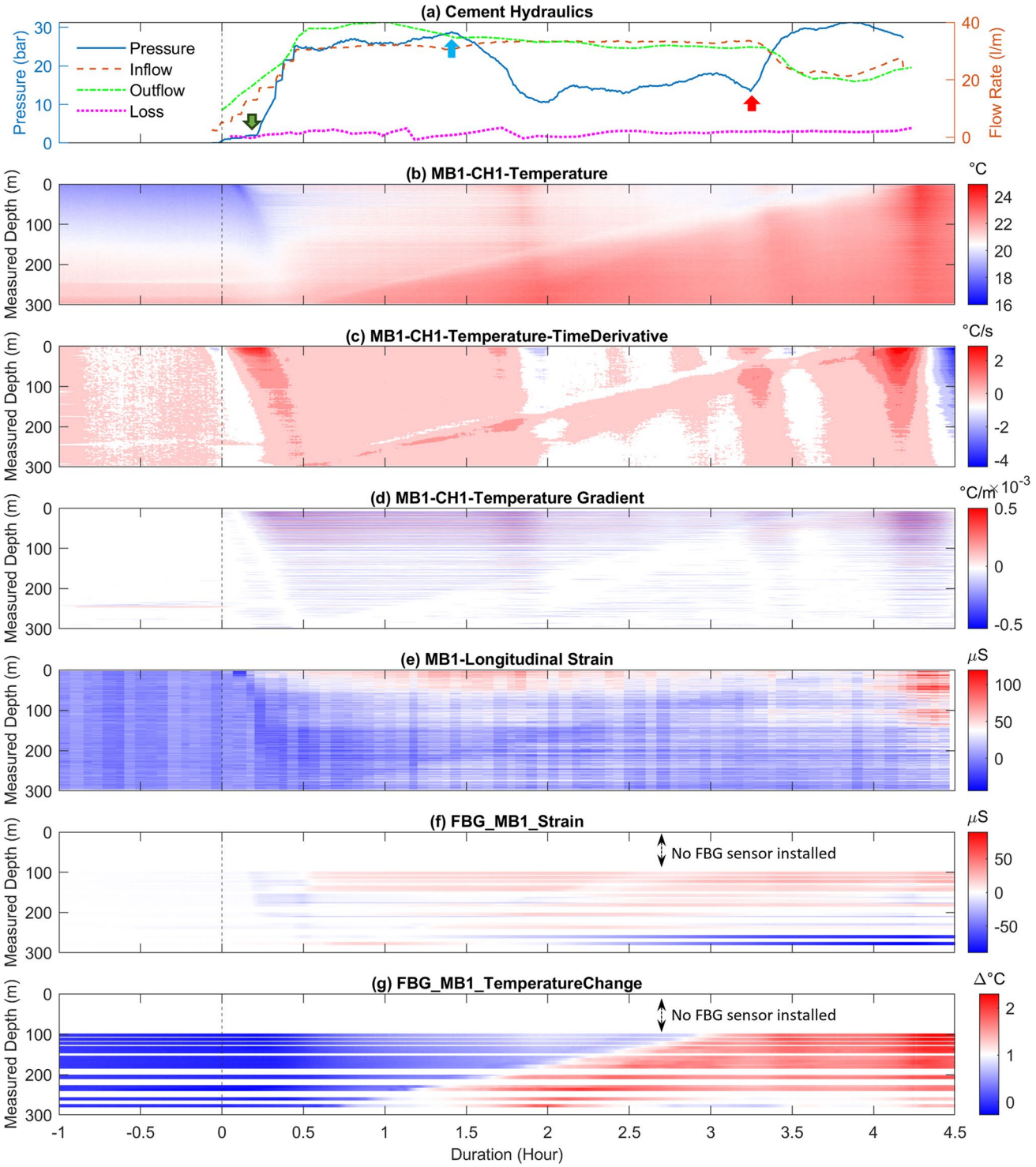

Fig. 5 MB1 monitoring during the cementation: **a** the cement injection hydraulics (arrows mark different phases of cement injection), **b** temperature (DTS), **c** temperature's time derivative and **d** temperature gradient, **e** longitudinal deformations recorded using DSS, **f** strain magnitudes recorded by FBG sensors, and **g** temperature changes recorded by FBG sensors. The recordings from each FBG sensor are presented with a ribbon at the corresponding depth of the sensor (width of the ribbon is not in scale to the length of the FBG sensors). The start of the cement injection is marked with the black dashed line in all plots

the outflow becomes slightly lower than the inflow, indicating a continuous but relatively stable loss of cement into the formation. This suggests a potential total cement loss of 360 l, which is relatively small compared to the total volume of injected cement, which is approximately 7300 l. After pumping around 6700 l of cement (slightly above the total volume of MB1, which is 6500 l) over approximately 4 h, low-density cement starts coming out of the outflow line. As a result, we decided to continue pumping an additional 600 l of highly viscous LCM cement. This brought the returned cement's density up to 1.6 g/cm^3. Subsequently, we stopped the cementing operation and shut in the wellhead. There were no indications of cement loss to ST2 during the operation. The distributed temperature profile during the cementation (Fig. 5b) clearly shows the onset of the thermal anomalies along the wellbore with the start of the cement injection. The injection of the cement through the central tubing is associated with an immediate cooling effect that can be spotted at the upper part of the wellbore, which almost uniformly moves downward. The arrival of the cement front in the annulus at the bottom of the wellbore manifests as a sharp thermal contrast, with elevated temperature. The advancement of the cement front can also be observed with larger contrast from the time derivative of temperature (Fig. 5c) and temperature gradient (Fig. 5d), for which, the temperature profiles are smoothed using the Savitzky–Golay filter with smoothing windows of 73 in time (ca. 24 min) and 54 in depth (ca. 6.75 m), respectively. The already identified flow zones from the logging at the depths of 244 m and 278 m can be observed in the time-derivative plots (Fig. 5c) with earlier temperature increase at the corresponding flow zones upon the arrival of the cement. In addition, the above-mentioned flow zones show as strong deflections in cement front's temperature profile in the gradient plot (Fig. 5-(d)), which also shows the flow zone at the depth of 244 m, even before the start of the cement injection. Shortly after the completion of the cementation operation, based on the temperature as well as its time-derivative profiles (Fig. 5b, c), a sharp temperature increase can be observed almost along the full wellbore, which dissipates within a few minutes.

The longitudinal strain magnitudes along MB1 recorded using the DSS during the cement injection are shown in Fig. 5e. Alternating patterns of expansive and compressive deformation along the wellbore depth can be observed from the DSS results, which can be explained by differences between the thermal properties of the DSS cable with that of the central injection pipe, to which it is clamped. The advancement of the cement slurry inside the central injection rod as well as in the annulus can be observed from the recorded strain profile, which is consistent with the temperature evolution recorded by DTS (Fig. 5b–d). The DSS measurements are, however, subjected to various influences, including drag forces by cement slurry exerted on the outside of the cable's corrugated coating, buoyancy effects caused by different fluid densities and thermal expansion/contraction of the cable.

The strain and temperature changes measured by the FBG sensors along MB1 during the cement injection are shown in Fig. 5f, g, respectively. As can be seen in the figures, the movement of the cement inside the injection tubing at the early stage of slurry pumping does not cause notable deformation nor temperature changes. This is due to the decoupling between the FBG sensors and the central tubing after the installation (see Introduction for details). On the other hand, as soon as the cement enters the annulus at the bottom of the wellbore, the temperature changes recorded by FBG sensors almost immediately show signatures of cement arrival, based on which, the temporal advancement of the cement front in the annulus can be closely monitored. In addition, the recorded temperature change profiles from FBG sensors show a slight oscillatory pattern superimposed on the general heating trend along the wellbore, which was also detected with DTS, but only partially due to their lower resolution compared with FBG sensors. The strain levels recorded by FBG sensors along the wellbore do not show major deformation from the wellhead to the depth of 237.3 m (see Fig. 5f). However, the two deepest FBG sensors at the depths of 260.3 m and 277.3 m show significant compression, in particular at the later stages of the cement injection. The compression starts as soon as the cement injection pressure reaches approximately 25 bar (see Fig. 5a), and continues until the final stage of the cement injection.

Monitoring after cementation

The thermo-hydro-mechanical response of MB1 is monitored for a time period of 7 days after the completion of the cementation operation to catch the four different phases of the cement-hardening process.

The recorded wellhead pressure after wellhead closure is presented in Fig. 6a. The starting time of the plots corresponds to approximately 18 min after stopping the cement injection, during which the monitoring systems' settings were adjusted for longer term monitoring of the wellbore. In order to evaluate any potential correlation between the wellhead pressure with the cement-hardening process, the wellbore temperature change, averaged over the full length of the wellbore (computed based on DTS measurements) is also plotted in the figure, assuming that the wellbore wall's irregularities does not affect averaged temperature magnitudes. As can be seen from the figure, the recorded pressure remains low, with a slight increase of approximately 0.01 bar per hour, for about nine hours after the wellhead closure. Shortly after wellhead closure, a continuous decline in the average temperature profile can be noted, corresponding to

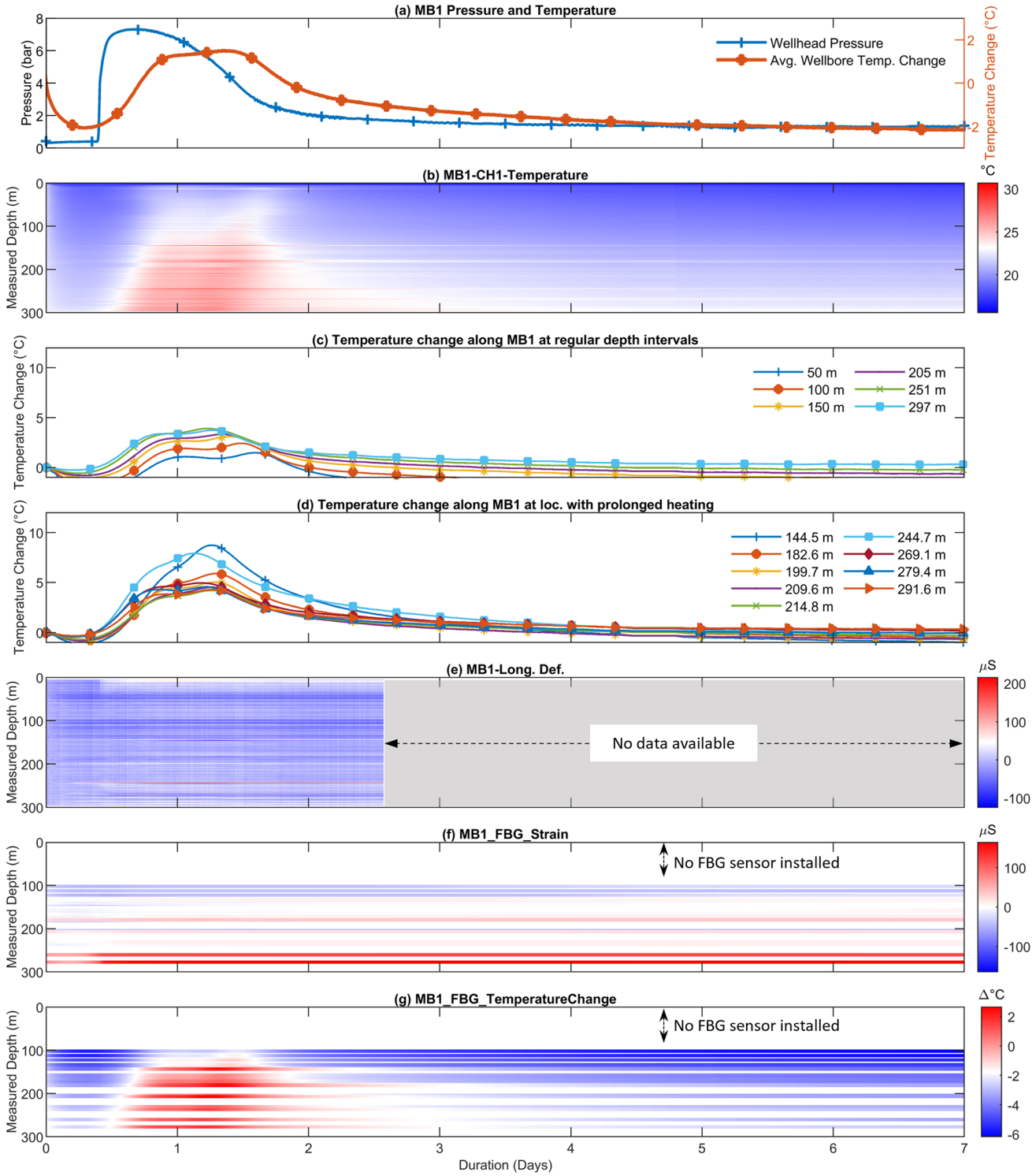

Fig. 6 Results from the installed monitoring systems in MB1 during 7-day observation period after the completion of the cementation: **a** the cement pressure as well as the average wellbore temperature, **b** distributed temperature profile (DTS) along the depth, **c** temperature changes at regular intervals (every 50 m, ± adjustments to avoid clamped sampling locations) extracted from DTS, **d** the temperature profile at zones identified with prolonged heating phase after cement placement (extracted from DTS), **e** strain profile along depth measured using DSS (measurements stopped about 60 h after the beginning of the monitoring period due to technical issues), **f** the strain profiles at sensor locations recorded using FBG, and **g** the temperature change at sensor locations recorded using FBG. Each FBG sensor is presented with a ribbon at the corresponding depth of the sensor (width of the ribbon is not in scale to the length of the FBG sensors)

the "slow reaction period" (see "Introduction"). The temperature's decreasing trend, however, reverses about 5 h after wellhead closure with the initiation of "acceleration period". At about 2.5 h of temperature increase, the wellhead pressure (which has been almost constant) undergoes a sharp increase, reaching 7.3 bar in less than three hours, after which it starts to level off and consequently decline to almost stabilize at about 1.4 bar within 4 days. The decline in temperature, however, starts significantly later than the corresponding trend in pressure (with a delay of about 16 h), marking the "deceleration period".

The distributed temperature profile in MB1 after wellhead closure—recorded with DTS—is presented in Fig. 6b. As shown in the figure, between 6 and 8 h after the cement placement (depending on the depth), the temperature starts to increase along the whole wellbore. In general, the deeper the observation point, the earlier the heating process starts and the more extended its duration. The temperature increase continues for about 1 day followed by a gradual decrease. However, at a number of locations along the wellbore, it is observed that the heating phase continues for several days, in particular, at depths of 144.5 m, 182.6 m, 199.7 m, 209.6 m, 214.8 m, 244.7 m, 269.1 m, 279.4 m and 291.6 m. At six of these depths, major flow zones have already been identified based on geophysical well logs. Figure 6c presents the corresponding temperature profiles at regular intervals (every 50 m, with minor adjustments to avoid collocation of the fiber clamping locations with the sampling points, if needed) in MB1. The temperature profile follows the average heating pattern of the wellbore, whereas Fig. 6d shows the temperature at the nine depths already been identified with prolonged heating phase (above mentioned). The "slow reaction period" can be clearly identified with a temperature decline in all sampled depths along MB1, including both regularly sampled as well as the depths with prolonged heating. The rate of heat generation, is, however, significantly larger in the locations with prolonged heating phase, compared with the regularly sampled intervals. The maximum temperature change recorded at regularly sampled intervals varies approximately between 3.4 °C and 5 °C, in contrast to a corresponding range of 5.2 °C to 10.1 °C in the locations with prolonged heating phase. The observed heat generation during accelerating phase is also hallmarked with two local temperature peaks, which is consistent with typical behavior of the cement gel during hardening phase (Bullard et al. 2011). However, the comparison between laboratory measurements of heating during cement hardening with presented observation in this study can only be qualitative, since the generated heat in the wellbore is continuously exchanged with wellbore's wall/rock volume.

The longitudinal strain along the wellbore recorded by DSS after the wellhead closure is presented in Fig. 6e. The DSS measurements stopped inadvertently, about 60 h after wellhead closure for technical reasons. A number of major strain anomalies can be observed, approximately at the depths of 144 m, 244 m, 270 m, 277 m, 286 m and 291 m, all of which manifest in the form of tensile deformation in the range of 50 με to 200 με. The anomalies start during the first day after the completion of the cementation operation and following a slight- and brief-recovery, the tensile deformations remain almost constant for the rest of the observation period.

The strains and temperature change profiles recorded by the FBG sensors in MB1, smoothed with Savitzky–Golay filter with a smoothing window of 30 s, are shown in Fig. 6f, g, respectively. Over the first few hours after the wellhead closure, the FBG sensors consistently show a slight compressional deformation. Then, a reverse in deformation pattern can be observed in almost all FBG sensors by the start of the "acceleration period", which is consistent with the temperature profile (Fig. 6b). In particular, the two deepest FBG sensors at the depths of 260.3 m and 277.3 m, show notable extensions, evidencing a maximum extension of 118 με and 165 με, respectively, after which the recorded extensions only slightly recover towards the end of the 7-day period. The extensional deformation associated with the "acceleration period" in three of the FBG sensors, namely at depths of 102.4 m, 122.4 m, and 157.3 m, initiated with a delay of 2–3 days, compared with other sensors. A single FBG sensor at the depth of 204.4 m does did not show notable extensional deformation by the end of the 7-day monitoring period. The temperature change profile recorded by the FBG sensors in MB1 (Fig. 6g) shows the heat generation associated with "acceleration period" during cement hardening that continues for approximately 12 h, after which the generated heat starts to dissipate into the formation (via the borehole wall). The pattern is also consistent with the observations from the DTS (see Fig. 6b).

Discussions

Several previous studies have successfully applied DTS and DSS technologies to various extents in wellbore integrity monitoring, particularly during cementation operations. This study, however, provides novel contributions compared with the prior works. One of the primary novelties of the presented study is the integrated approach, which combines pressure sensors with DTS, DSS and FBG sensing technologies. Notably, in the current study, FBG sensors provided us with the added benefit of measuring at high frequencies, specifically at 10 Hz, allowing for almost immediate and real-time detection of the evolution of the top of the cement within the wellbore (as shown in Fig. 5g). Another notable aspect of this research is its in-depth evaluation of the thermo-hydro-mechanical behavior of the wellbore during

both cement injection and cement-hardening phases, in order to shed light on the dynamic interactions between the cement and the surrounding geologic formations, involving hydraulic shortcuts and major inflow zones. In addition, the installed monitoring system is observed to provide valuable information about the hydrogeological setting of the wellbore both before- and after cementation. It is also noteworthy to mention that our study was carried out within a thoroughly characterized rock volume, accompanied by a comprehensive inventory of fractures within the wellbore. This extensive knowledge significantly supported our interpretations and provided us with the necessary tools to analyze monitoring results using fiber optics. Comprehensive discussions regarding the observations during and after the cementation operation are provided in the following sections.

During cement injection

By the start of the cement injection in MB1, the flow of cement into the wellbore is supported by the higher density of the cement slurry in the injection rod, which results in only a slight increase in injection pressure. Upon arrival of the cement slurry in the annulus, the pump needs to overcome the continuously increasing weight of the cement column in the annulus, which causes notable increase in the injection pressure due to elevated friction.

The almost linear advancement of the cement front within the annulus that was detected by temperature as well as its time derivative from DTS is consistent with the relatively constant cement injection rate, corroborating the absence of major cement loss. However, the presence of major inflow zones along the wellbore leads to a relatively blunt border between the cement front's temperature with that of the wellbore fluid, which can be seen in particular at the depths of 144 m and 244 m from the temperature's time-derivative profile (Fig. 5c). On the other hand, the temperature gradient plot is not significantly influenced by the distortion of the cement–water border. During cement injection, the maximum recorded temperature increase along the wellbore occurs approximately at the depth of 244 m, at which a natural inflow zone has already been identified based on logging results as heat loss zone. Therefore, the corresponding temperature increases during the cementation can be attributed to the blockage of the inflow zones by the cement column, which leads to equilibrating the thermal anomaly followed by a sharp increase in the temperature.

The observed oscillatory pattern of temperature in the annulus upon arrival of the cement, in particular recorded by the FBG sensor, can be attributed to multiple factors, including (a) the imminent start of "initial reaction" period within the cement slurry inside the injection pipe, (b) heat exchange between the cement slurry and the wellbore wall, and (c) the presence of localized thermal anomalies. In particular, the "initial reaction" phase will be difficult to exactly identify because of its rapid initiation and dissipation. The utilization of FBG sensors in our study proved to be of significant value due to their high sampling frequency, specifically 10 Hz. This high sampling rate allowed us to promptly detect thermal anomalies within the wellbore. This capability is particularly advantageous when compared to the DTS system, which operates at a much lower sampling frequency of 0.2 Hz. The lower sampling frequency of the DTS system can potentially convolute various thermal effects over the sampling period, making it challenging to distinguish between different thermal effects.

The observed deformations from FBG sensors during the cement injection can be due to the influence of injection-related processes, such as buoyancy effect, which is supported by the fact that the recorded compressions in the two deepest FBG sensors were partially reversed at the later stages of injection, when the cement injection pressure decreased significantly due to the injection of a different cement slurry. The dragging force caused by the viscous cement around annulus, however, does not have a major impact on the FBG sensor recordings, since no significant anomaly has been detected immediately after the injection stops.

The strain values recorded with DSS during the cement injection are mainly dominated by the thermal effects, either direct contact between cement and cable within the annulus, or indirect contact between cable in the annulus and the cement slurry inside the injection rod.

During cement hardening

The abrupt increase in wellhead pressure shortly after wellhead closure can be due to the interactions between the cement loss, back-pressure buildup from the reservoir, and thermally induced expansion. When the cement loss stops (by the Lost Circulation Materials—LCM (Boukadi et al. (2004))), the increase in—back-pressure as well as—the cement temperature elevates the wellbore pressure. However, the temperature increase, which is due to the initiation of the cement-hardening process, follows the sharp increase in pressure, which implies that the effect of the back-pressure is more significant than the thermal expansion of the slurry. The consequent decline of the wellbore pressure and stabilization at about 1.2 bar, affirms that the cement-hardening process ultimately resulted in net shrinkage. At this point, the wellbore is sealed by the low permeable and hardened cement column, and the transfer of pressure from the fracture zones to the wellhead is limited and very slow.

The DTS results during cement hardening show that the accelerated heat generation phase consistently starts earlier in the deeper parts of the wellbore and persists for

an extended duration, which is due to the fact that corresponding elevated in-situ temperature accelerates the hydration reactions (Thomas et al. 2009). The results also show that all, except one of the major flowing zones detected with logging, manifested as prolonged and elevated temperature anomalies during cement hardening, deviated from the general pattern of the wellbore. Given that almost all identified flow zones from well logs were characterized as heat loss zone, it can be inferred that such characteristic of the flow has negligible influence on the observed temperature profile during hardening. The observed temperature anomalies at the flow zones may be attributed to two potential causes:

(I) The presence of breakouts or highly permeable structures can cause a larger accumulation of cement. Specifically, in the case of wellbore breakouts, which mainly occur between depths of 150–210 m in MB1, they do not significantly affect the temperature profile. In addition, if there had been a substantial loss of cement into permeable structures, we would have expected to see a gradual and bidirectional expansion of the thermal anomaly along the wellbore trajectory over time. This is because the cement that penetrates these permeable fractures or faults would heat up their sidewalls, leading to observable changes in the temperature profiles. However, such changes have not been observed in the temperature.

(II) The flowing zones acting as water reserves during the cement-hardening process: it is known that if the cement hardening proceeds in adiabatic environment without external source of water, the internal relative humidity (RH) of the cement decreases, leading to "self-desiccation" as well as shrinkage in total volume of the cement, whereas, continuous supply of water to the cement gel during the hardening phase promotes the cement hydration, and therefore results in a longer heat generation (Wong 2018; Bullard et al. 2011). Since in the wellbore, the continuous supply of water to the cement in the vicinity of the flowing structures is present, it can be inferred that the observed thermal anomalies are mainly caused by the presence of permeable structures in the vicinity of the anomaly. The DTS measurement during cement hardening were not only able to reveal the location of almost all flow zones detected with geophysical logs, but also showed similar elevated temperature patterns at several other locations. This innovative approach to interpret cement temperature monitoring results not only provides valuable insights into the presence of previously undetected, potentially weaker flow zones but may also underscores its distinct advantage in obtaining critical information that traditional geophysical well logs may overlook. The significant expansion of about 200 με, recorded by DSS during cement hardening at the approximate depth of 244 m, can be attributed to the significant compliance and expansion of the corresponding structure because of the effect of reservoir back-pressure.

The delayed initiation of the extensional deformation during the "acceleration period" that was marked by three FBG sensors can be due to dilution of the cement patches in the vicinity of the noted sensors, especially that their shallow depths imply that the corresponding cement volumes are from the early stage of cement injection, potentially before the cement column pressure as well as the LCM could block the inflows from permeable structures. It is noteworthy to mention that such strain anomalies detected by FBG sensors were not particularly detected by the DSS sensor due to its lower measurement resolution and accuracy.

It is also noteworthy to mention that understanding the permeability of cement and its relationship with stress changes is important in the context of wellbore integrity assessment. In our study, we focused on evaluating wellbore integrity during and after the cementation process, with an emphasis on addressing the presence of micro-annuli and channels within the cement matrix. Although direct laboratory permeability data for the cement used were unavailable, existing literature (Skadsem 2022; Al Ramadan et al. 2019; Schlumberger 2005, Goode 1962) suggests a typical range of 0.001–0.1 micro-Darcy for well-cured bentonite cement, a range we believe our cement likely falls within. However, the micro-annuli and channels may exhibit higher permeabilities, potentially impacting wellbore integrity. Hence, our study aimed to optimize cement recipes and placement procedures to mitigate these concerns. Importantly, our integrity monitoring results indicated no evidence of major compromised cement quality, confirming the robust wellbore integrity. Regarding the permeability–stress relationships of cement, although we did not investigate them in this study, we acknowledge their significance, especially in scenarios such as reservoir pressurization following cementation or during injection experiments in nearby wellbores (Min et al. 2004; Davies and Davies 2001). It is, however, expected that the stress changes resulting from geomechanical effects in the BULGG reservoir volume will likely be more localized, particularly at the intersection of the wellbore with fractures and faults. Consequently, we anticipate that these localized stress changes are unlikely to significantly impact the overall wellbore integrity. Estimating changes in cement permeability due to strain, considering the complex interactions and contrast in mechanical properties and stress changes within both the cement and reservoir, presents a potential path for future research. This understanding can enhance wellbore integrity assessments and also can improve our evaluations of cement performance.

Conclusion

The installed wellbore monitoring system at BULGG provided us with detailed information at different stages of the wellbore development, including, before, during, and after

the cementation, at high spatial and temporal resolution. The multi-component installation within the same borehole gave us a unique opportunity to evaluate and compare the observations of different monitoring techniques during cementation, in particular, from DSS, DTS and FBG. As it was shown in the results, the cement injection and hardening process are associated with complex thermo-hydro-mechanical changes within the cement slurry and wellbore. The application of different fiber-optic technologies provided us with the means to shed light on such multi-physical phenomena by monitoring the cement placement and hardening process at a wide range of spatial/temporal resolution. It was found that each of the utilized techniques can provide us unique and complementary set of information about the involved processes.

The DTS provides us the information about temporal dynamics of the cement front during the cement injection as well as the qualitative information regarding the hydraulic properties of the major inflow zones in the wellbore after the cement placement. The post-processing of the temperature profiles, in particular, the time-derivative and the gradient, reveals extra details with larger contrast (compared with the temperature data itself) during cementation. The temperature's time derivative can follow the cement front's advancement within the wellbore during the cement injection. The temperature gradient, on the other hand, is capable of detecting the location of thermal anomalies due to the presence of inflow zones. It is observed that the thermal anomalies detected after the cement placement may be used to identify the presence of the inflow zones within the wellbore that act as continuous source of water to promote the cement-hardening reactions associated with elevated temperature. The number of detected flow zones in the wellbore based on the prolonged heating phase after cement placement exceeds even beyond the resolution of the conventional well logs. This has the potential to help us to better characterize the hydrogeological settings of the target reservoir and constrain the observations from the geophysical well logs, in particular the presence of open fractures/faults even after the wellbore is sealed with the cement.

The DSS measurements during the cement injection mainly represent the thermal effects caused by the injection of the cement slurry with a different temperature than the in-situ water, therefore, following the same pattern as the DTS. After the cement placement, the fracture/fault zones with relatively large compliance undergo major tensile deformation due to the back-pressure from the reservoir. Such anomalies can be identified efficiently using the DSS, thanks to its full coverage of the wellbore in terms of detecting relatively large strain anomalies.

The FBG sensors can immediately detect the arrival of the cement front within the wellbore. The temperature measurements from FBG sensors during the cement-hardening phase accurately capture different phases of the cement hardening, both in terms of deformation and temperature, owing to their superior precision and enhanced accuracy, which offer a distinct advantage over the DSS system. The FBG sensors are also able to detect the potential locations of the low-quality cement (diluted during injection) along the wellbore. The localized nature of the measurements carried out by FBG sensors, however, limits their capability to detect all existing anomalies along the wellbore. This necessitates a comprehensive analysis of the well logs during the planning phase before sensor installation, in order to select the optimal locations of the FBG sensors. The observations also imply that having both DSS and FBG sensors can be beneficial, as they complement each other and provide comprehensive coverage, sampling frequency, and accuracy, effectively addressing the potential gaps in anomaly detection along the wellbore.

As a future work, the measurements from the installed monitoring system in the wellbore will be used for longer term analyses of the evolution of wellbore integrity under thermo-hydro-mechanical effects, especially during the stimulation/circulation experiments.

Supplementary Information The online version contains supplementary material available at https://doi.org/10.1007/s12665-024-11451-2.

Acknowledgements The BULGG is supported by the Swiss Federal Office of Energy (SFOE) (project VALTER), the EU Horizon 2020 (project DESTRESS), the EU initiative Geothermica—EraNet (projects ZoDrEx and SPINE), the Werner Siemens-Stiftung (project MISS), ETH Zurich and ERC (project SyG FEAR). We appreciate the inputs from Michael Vorwerk und Christian Anderrüthi from SIKA for cement slurry design and analyses. We thank NAGRA and Prof. Simon Loew for providing us with the DTS interrogators at different stages of this investigation. We thank GEO ENERGIE SUISSE team, especially Peter Meier, Francisco Serbeto, and Falko Bethmann for their support. We would also like to acknowledge and thank all members of the BedrettoLab team for their invaluable contributions and assistance throughout this project.

Author contributions Nima Gholizadeh Doonechaly, Andreas Reinicke and Frank Fischli wrote the main manuscript text. All the co-authors contributed to the writing and revision of the paper. Katrin Plenkers, Anne Obermann, Andreas Reinicke, Marian Hertrich and Nima Gholizadeh Doonechaly carried out the sensor designs and installations as well as the cementation operation. Hansruedi Maurer, Stefan Wiemer, and Domenico Giardini supervised the project.

Funding Open access funding provided by Swiss Federal Institute of Technology Zurich The BULGG experiments are funded by the Swiss Federal Office of Energy (SFOE) (project VALTER), by the EU Horizon 2020 (project DESTRESS), by the EU initiative Geothermica—EraNet (projects ZoDrEx and SPINE), the Werner Siemens-Stiftung (project MISS) and by ERC (project SyG FEAR).

Availability of data and materials The datasets generated/analyzed during the current study are available from the corresponding author on reasonable request.

Declarations

Conflict of interest The authors have no competing interests to declare that are relevant to the content of this article.

References

Al Ramadan M, Salehi S, Kwatia G, Ezeakacha C, Teodoriu C (2019) Experimental investigation of well integrity: annular gas migration in cement column. J Petrol Sci Eng 179:126–135. https://doi.org/10.1016/j.petrol.2019.04.023

Batcheller GW (2013) Cement evaluation challenges in horizontal wells—guidelines for providing meaningful data. In: SPE Production and Operations Symposium. https://doi.org/10.2118/164513-ms

Boukadi F, Yaghi B, Al-Hadrami H, Bemani ALI, Babadagli T, De Mestre P (2004) A comparative study of lost circulation materials. Energy Sources 26(11):1043–1051. https://doi.org/10.1080/00908310490494612

Bullard JW, Jennings HM, Livingston RA, Nonat A, Scherer GW, Schweitzer JS, Scrivener KL, Thomas JJ (2011) Mechanisms of cement hydration. Cem Concr Res 41(12):1208–1223. https://doi.org/10.1016/j.cemconres.2010.09.011

Cao P, Karpyn ZT, Li L (2013) Dynamic alterations in wellbore cement integrity due to geochemical reactions in CO2-rich environments. Water Resour Res 49(7):4465–4475. https://doi.org/10.1002/wrcr.20340

Chen S, Jin J-Z, Shen J, Guo X, Wang L (2023) Monitoring evolution of temperature and strain in cement sheath using embedded optical fiber Bragg gratings. SPE J 28(01):19–31. https://doi.org/10.2118/212264-PA%JSPEJournal

CTEMPs (2015) DTS data processing. Retrieved from https://ctemps.org/data-processing, Accessed 2 Nov 2023

Dakin JP, Pratt DJ, Bibby GW, Ross JN (1985) Distributed optical fiber raman temperature sensor using a semiconductor light-source and detector. Electron Lett 21(13):569–570. https://doi.org/10.1049/el:19850402

Davies JP, Davies DK (2001) Stress-dependent permeability: characterization and modeling. SPE J 6(02):224–235. https://doi.org/10.2118/71750-PA%JSPEJournal

Goode JM (1962) Gas and water permeability data for Some Common Oilwell Cements. J Petrol Technol 14(08):851–854. https://doi.org/10.2118/288-PA%JJournalofPetroleumTechnology

Horiguchi T, Shimizu K, Kurashima T, Tateda M, Koyamada Y (1995) Development of a distributed sensing technique using Brillouin scattering. J Lightwave Technol 13(7):1296–1302. https://doi.org/10.1109/50.400684

Hurtig E (1993) Borehole temperature measurements using distributed fibre optic sensing. Sci Drill 3:283–286

Kamal SZ (2014) Fiber optic sensing: evolution to value. In: SPE Intelligent Energy Conference & exhibition, society of petroleum engineers. https://doi.org/10.2118/167907-MS

Keller F, Schneider TR (1982) Geologie und geotechnik. Der Furka-Basistunnel: Zur Eröffnung Am 25:512–520. https://doi.org/10.5169/seals-74820

Kiran R, Teodoriu C, Dadmohammadi Y, Nygaard R, Wood D, Mokhtari M, Salehi S (2017) Identification and evaluation of well integrity and causes of failure of well integrity barriers (A review). J Nat Gas Sci Eng 45:511–526. https://doi.org/10.1016/j.jngse.2017.05.009

Kragas TK, Williams BA, Myers GA (2001) The optic oil field: deployment and application of permanent in-well fiber optic sensing systems for production and reservoir monitoring. In: SPE Annual Technical Conference and Exhibition, Society of Petroleum Engineers. https://doi.org/10.2118/71529-MS.

Lindsey NJ, Martin ER (2020) Fiber-optic seismology. Annu Rev Earth Planet Sci. https://doi.org/10.1146/annurev-earth-072420-065213

Ma X, Hertrich M, Amann F, Bröker K, Gholizadeh DN, Gischig V, Hochreutener R, Kästli P, Krietsch H, Marti M, Nägeli B, Nejati M, Obermann A, Plenkers K, Rinaldi AP, Shakas A, Villiger L, Wenning Q, Zappone A, Bethmann F, Castilla R, Seberto F, Meier P, Driesner T, Loew S, Maurer H, Saar MO, Wiemer S, Giardini D (2022) Multi-disciplinary characterizations of the Bedretto-Lab—a new underground geoscience research facility. Solid Earth 13(2):301–322. https://doi.org/10.5194/se-13-301-2022

Manceau JC, Tremosa J, Audigane P, Lerouge C, Claret F, Lettry Y, Fierz T, Nussbaum C (2015) Well integrity assessment under temperature and pressure stresses by a 1:1 scale wellbore experiment. 51(8): 6093–6109. https://doi.org/10.1002/2014WR016786

Micron Optics I. (2014) FBG Total Strain Thermal Considerations | Five Steps to Meaningful Strain Data Technical Note 1025 | Revision 2014.1.31.1.

Min K-B, Rutqvist J, Tsang C-F, Jing L (2004) Stress-dependent permeability of fractured rock masses: a numerical study. Int J Rock Mech Min Sci 41(7):1191–1210. https://doi.org/10.1016/j.ijrmms.2004.05.005

Morris W, Criado MA, Robles J, Bianchi G (2003) Design of high toughness cement for effective long lasting well isolations. In: SPE Latin American and Caribbean Petroleum Engineering Conference, Society of Petroleum Engineers

Pardue G, Morris R (1963) Cement bond log-a study of cement and casing variables. J Petrol Technol 15(05):545–555. https://doi.org/10.2118/453-PA

Pearce JG, Rambow FHK, Shroyer W, Huckabee P, de Jongh H, Dria DE, Childers BA, Hall TS, Dominique T (2009) High resolution, real-time casing strain imaging for reservoir and well integrity monitoring: demonstration of monitoring capability in a field installation. SPE Annual Technical Conference and Exhibition. https://doi.org/10.2118/124932-ms.

Plenkers K, Reinicke A, Obermann A, Gholizadeh Doonechaly N, Krietsch H, Fechner T, Hertrich M, Kontar K, Maurer H, Philipp J, Rinderknecht B, Volksdorf M, Giardini D, Wiemer S (2023) Multi-disciplinary monitoring networks for mesoscale underground experiments: advances in the Bedretto Reservoir Project. Sensors 23(6):3315. https://doi.org/10.3390/s23063315

Prognos A (2012) Die Energieperspektiven für die Schweiz bis 2050. Energienachfrage und Elektrizitätsangebot in der Schweiz 2050

Raab T, Reinsch T, Cifuentes SRA, Henninges J (2019) Real-Time well-integrity monitoring using fiber-optic distributed acoustic sensing. SPE J 24(5):1997–2009. https://doi.org/10.2118/195678-Pa

Rast M, Galli A, Ruh JB, Guillong M, Madonna C (2022) Geology along the Bedretto tunnel: kinematic and geochronological constraints on the evolution of the Gotthard Massif (Central

Alps). Swiss J Geosci 115(1):1–31. https://doi.org/10.1186/s00015-022-00409-w

Reinsch T, Henninges J, Ásmundsson R (2013) Thermal, mechanical and chemical influences on the performance of optical fibres for distributed temperature sensing in a hot geothermal well. Environ Earth Sci 70(8):3465–3480. https://doi.org/10.1007/s12665-013-2248-8

Schenato L (2017) A review of distributed fibre optic sensors for geo-hydrological applications. Applied Sci-Basel 7(9):896. https://doi.org/10.3390/app7090896

Schlumberger (2005) Memory Slim Cement Bond Logging Tool, https://www.slb.com/-/media/files/fe/brochure/memory-slim-cblt-br (visited on 01.11.2023). (04-PR-086).

SFOE (2021) Energy Strategy 2050. Swiss Federal Office of Energy, https://www.bfe.admin.ch/bfe/en/home/policy/energy-strategy-2050.html, Last modified on 16.12.2021, Visited on 01.11.2023.

Shakas A, Wenning Q, Bröker K, Escallón BD, Behnen K, Hertrich M (2021) Borehole Trajectories for VALTER volume. Bedretto Lab, ETH Zurich. https://doi.org/10.3929/ethz-b-000517623

SIKA (2023) Sika UW Compound-100. Retrieved from : https://che.sika.com/dam/dms/ch01/g/sika_uw_compound-100.pdf, Accessed 2 Nov 2023

Silixa XT (2023) Silixa's ruggedised distributed temperature sensor, XT-DTS. Silixa LTD, Retrieved from https://silixa.com/technology/xt-dts/, Accessed 2 Nov 2023

Silixa ULTIMA (2023) Distributed temperature sensing—ULTIMA DTS. Silixa LTD, Retrieved from https://silixa.com/technology/ultima-dts/, Accessed 2 Nov 2023

Skadsem HJ (2022) Characterization of annular cement permeability of a logged well section using pressure-pulse decay measurements. J Energy Resour Technol. https://doi.org/10.1115/1.4053709

Thomas JJ, Jennings HM, Chen JJ (2009) Influence of nucleation seeding on the hydration mechanisms of tricalcium silicate and cement. J Phys Chem C 113(11):4327–4334. https://doi.org/10.1021/jp809811w

Thomas S, Smith CH, Williams BW, Hamilton L (2016) Ultrasonic-Log response in lightweight-cement conditions. SPE Drilling Completion 30(04):326–333. https://doi.org/10.2118/171612-PA

Wenning QC, Gholizadeh Doonechaly N, Shakas A, Hertrich M, Maurer H, Giardini D, Team B, Serbeto F, Bethmann F, Dyer B, Castilla R, Meier P, Wiemer S (2022) Heat propagation through fractures during hydraulic stimulation in crystalline Rock. 56th U.S. Rock Mechanics/Geomechanics Symposium. https://doi.org/10.56952/arma-2022-2112

Wong HS (2018) Concrete with superabsorbent polymer. Eco-efficient repair and rehabilitation of concrete infrastructures. Elsevier, pp 467–499

Wu Q, Nair S, Shuck M, van Oort E, Guzik A, Kishida K (2017) Advanced distributed fiber optic sensors for monitoring real-time cementing operations and long term zonal isolation. J Pet Sci Eng 158:479–493. https://doi.org/10.1016/j.petrol.2017.08.072

Xue ZQ, Hashimoto T (2017) Geomechanical monitoring of caprock and wellbore integrity using fiber optic cable: strain measurement from the fluid injection and extraction field tests. In: 13th International Conference on greenhouse gas control technologies, Ghgt-13 114: 3305–3311. https://doi.org/10.1016/j.egypro.2017.03.1462.

Zhu HH, Shi B, Zhang CC (2017) FBG-Based Monitoring of Geohazards: Current Status and Trends. Sensors (basel) 17(3):452. https://doi.org/10.3390/s17030452